Acta Pharmaceutica Sinica B 2024;14(11):4962–4976

Chinese Pharmaceutical Association
Institute of Materia Medica, Chinese Academy of Medical Sciences

Acta Pharmaceutica Sinica B

www.elsevier.com/locate/apsb
www.sciencedirect.com

ORIGINAL ARTICLE

Multiepitope recognition technology promotes the in-depth analysis of antibody–drug conjugates

Yutian Lei [a,b,†], Yuan Shen [c,†], Feng Chen [a], Rui He [a], Zhang Zhang [a], Ying Zhou [a], Jin-Chen Yu [d], Jacques Crommen [a,e], Zhengjin Jiang [a,*], Qiqin Wang [a,*]

[a]*Institute of Pharmaceutical Analysis, College of Pharmacy/State Key Laboratory of Bioactive Molecules and Druggability Assessment/International Cooperative Laboratory of Traditional Chinese Medicine Modernization and Innovative Drug Development of Ministry of Education (MOE) of China, Jinan University, Guangzhou 510632, China*
[b]*School of Biomedical Engineering, Sun Yat-sen University, Shenzhen 518107, China*
[c]*Department of Clinical Pharmacy, Wuhan Children's Hospital (Wuhan Maternal and Child Healthcare Hospital), Tongji Medical College, Huazhong University of Science & Technology, Wuhan 430016, China*
[d]*Bio-Thera Solutions, Ltd, Guangzhou 510700, China*
[e]*Laboratory for the Analysis of Medicines, Department of Pharmaceutical Sciences, CIRM, University of Liege, Liege B-4000, Belgium*

Received 27 March 2024; received in revised form 8 May 2024; accepted 11 June 2024

KEY WORDS

Antibody–drug conjugate;
Multiepitope recognition strategy;
Affinity enrichment;
Biotransformation;
LC–MS

Abstract The dynamic tracking of antibody–drug conjugates (ADCs) in serum is crucial. However, a versatile bioanalytical platform is lacking due to serious matrix interferences, the heterogeneity and complex biotransformation of ADCs, and the recognition deficiencies of traditional affinity technologies. To overcome this, a multiepitope recognition technology (MERT) was developed by simultaneously immobilizing CDR and non-CDR ligands onto MOF@AuNPs. MERT's excellent specificity, ultrahigh ligand density, and potential synergistic recognition ability enable it to target the different key regions of ADCs to overcome the deficiencies of traditional technologies. The binding capacity of MERT for antibodies is ten to hundred times higher than that of the mono-epitope or Fc-specific affinity technologies. Since MERT can efficiently capture target ADCs from serum, a novel bioanalytical platform based on MERT and RPLC–QTOF-MS has been developed to monitor the

*Corresponding authors.
E-mail addresses: jzjjackson@hotmail.com (Zhengjin Jiang), qiqinxtu@163.com (Qiqin Wang).
[†]These authors made equal contributions to this work.
Peer review under the responsibility of Chinese Pharmaceutical Association and Institute of Materia Medica, Chinese Academy of Medical Sciences.

https://doi.org/10.1016/j.apsb.2024.06.007

dynamic changes of ADCs in serum, including the fast changes of drug-to-antibody ratio from 3.67 to 0.22, the loss of payloads (maytansinol), and the unexpected hydrolysis of the succinimide ring of the linker, which will contribute to clarify the fate of ADCs and provide a theoretical basis for future design. In summary, the MERT-based versatile platform will open a new avenue for in-depth studies of ADCs in biological fluids.

1. Introduction

Antibody−drug conjugates (ADCs), which combine the specificity of monoclonal antibodies (mAbs) with the potency of highly cytotoxic agents, have emerged as a new class of smart biopharmaceuticals for both solid and hematological malignancies[1−3]. However, to date, the clinical trials of 92 ADC candidates out of over 260 have had to be terminated because of intolerable toxicity and insufficient therapeutic efficacy[4,5]. It has been reported that less than 1%−2% of an ADC reaches the tumor in humans, while the remainder potentially causes unwanted off-target toxicities[6−8]. Moreover, the complex biotransformation of ADCs after administration to patients, including linker cleavage, payload deconjugation or metabolism, and antibody modifications, could reduce its bioactivity, and induce undesirable changes in pharmacokinetic (PK) properties, drug-to-antibody ratio (DAR), and immunogenicity[9,10], which could restrict their development[11]. Therefore, the dynamic tracking of DAR and biotransformation of ADCs in the blood circulatory system is of high interest for their early-stage development.

However, due to the uncontrollability of the conjugation process, highly heterogeneous ADCs commonly contain plenty of species with varying DARs as well as drugs attached at various conjugation sites[5,11−13]. Moreover, the analytical challenges are further increased due to the dynamic changes of DAR in the *in vivo* circulation, accompanied by the biotransformation of linkers, small molecule drugs and antibodies, and the serious matrix interferences of serum samples containing high homology IgGs (7−18 mg/mL)[14,15]. Even though enzyme-linked immunosorbent assay (ELISA) can provide total antibody concentration *in vivo*, it cannot monitor DAR and any structural information[16]. To cope with these challenges, immunoaffinity LC−HRMS was recently developed for ADC biotransformation assessment with excellent sensitivity, mass accuracy/resolution, and abundant structure information[14,17]. Nevertheless, some inherent limitations, including the requirement of biotinylated antigens or anti-idiotypic (anti-id) antibodies for ADC capture, the high manufacturing costs, instability, and low antibody binding capacity of immunoaffinity materials, need to be resolved[18]. Furthermore, some particular challenges for ADC analysis could happen if the epitope that is recognized by the antigen is modified or if the modifications (deamidation[19] isomerization[20] and oxidation[21]) of the key residues at the complementarity-determining region (CDR) of the antibody results in a loss of interaction between the drug and the immunoaffinity ligand[19,22−26]. Especially, the introduction of small molecule drugs can significantly enhance the steric hindrance between ADC and affinity ligands. Due to steric hindrance or low affinity, ADCs with different DARs may have different binding abilities to immunoaffinity materials, resulting in the loss of some key ADCs and affecting the analytical method accuracy[27−29]. For instance, Stephan et al. found that the increase of the small molecule drug load on the antibody could decrease the target anti-CD22-MCC-DM1 binding to the antigen[27,29]. How to overcome these immune recognition deficiencies of traditional affinity technologies and develop a reliable bioanalytical method remain major challenges.

Antigen mimotope peptides, which can specifically bind to the CDRs of the target mAb, were recently proposed as "surrogate antigens" for mAb recognition[18]. To date, few antigens (cluster of differentiation 20, epidermal growth factor receptor) mimotope peptides have been used to construct biosensors for precise monitoring of mAbs[30−32] as well as to develop affinity materials for the enrichment and modification analysis of mAbs in patient serum[15,33,34]. Although mimotope peptide-based affinity technology can overcome the high manufacturing costs and instability of the antigen[18] and even significantly improve the antibody binding capacity by combining it with composite microparticles[35], their mono-epitope recognition property could hardly overcome the above immune recognition deficiencies for ADC analysis.

Similar challenges also occur in the immune recognition of tumor cells by mAbs (Scheme 1). When the antigenic epitope on tumor cells is lost or mutated, the mAb is unable to produce an effective immune response, leading to an unexpected immune escape of tumor cells. Fortunately, bispecific antibodies (BsAbs), which can recognize two different epitopes, were successfully developed to overcome the immune escape of tumor cells by blocking two different signaling pathways simultaneously[36−38]. Inspired by BsAbs, a novel multiepitope recognition technology (MERT) was proposed for the first time to specifically bind to distinct regions [CDR and non-CDR in antigen-binding fragment (Fab)] of the target ADC. MERT was developed by simultaneously immobilizing a mimotope peptide (HH24) of human epidermal growth factor receptor 2 (HER2) and an aptamer (CH1S-6T) onto the surface of MOF@AuNPs (Scheme 1). The potential synergistic binding effects of these two ligands could enhance their binding ability towards the target ADC, improve the specificity and anti-fouling ability of MOF@Au@HH24@CH1S-6T, and thus overcome the immune recognition deficiencies of traditional affinity materials. These advantages were confirmed by comparison studies of MOF@Au@HH24, MOF@Au@CH1S-6T, and MOF@Au@HH24@CH1S-6T for antibody or ADC analysis. Considering that clinical samples are typically not available in the early-stage development of ADC candidates, *in vitro* serum models were used to evaluate ADC biotransformation and predict *in vivo* results[39]. Therefore, a novel bioanalytical platform for ADC subunit evaluation was then constructed by combining highly efficient RPLC−QTOF-MS with MERT. Moreover, the dynamic monitoring of DAR, drug load distribution (DLD), and

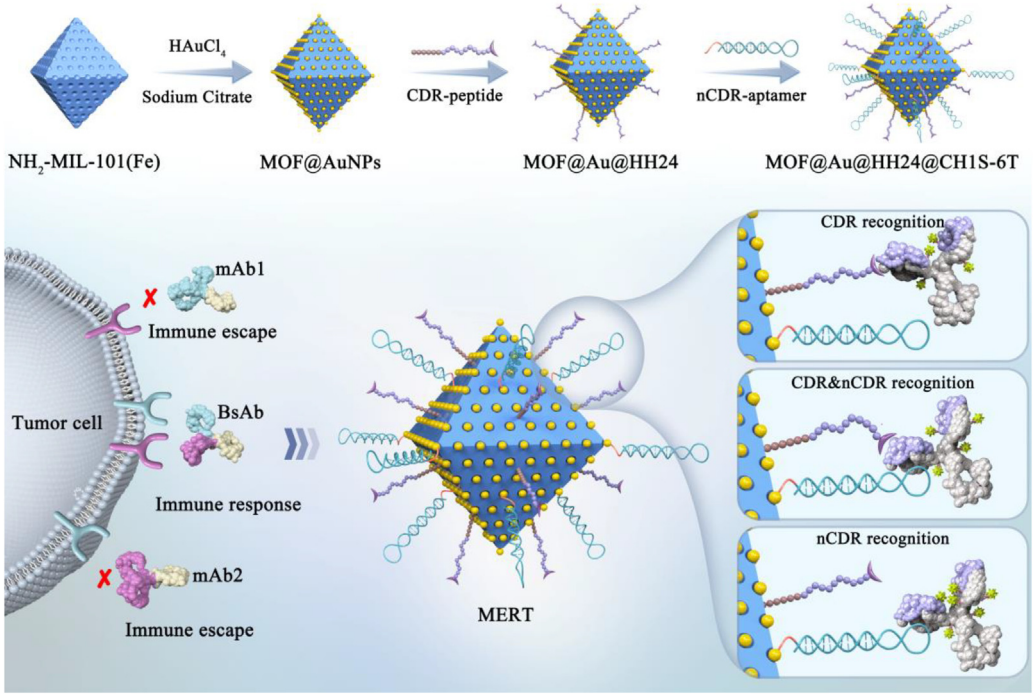

Scheme 1 Design diagram of the multiepitope recognition material (MOF@Au@HH24@CH1S-6T).

biotransformation of anti-HER2 ADC candidates in spiked human serum were performed using this bioanalytical platform.

2. Results and discussion

2.1. *Development of the multiepitope recognition material*

To fabricate a multiepitope recognition material with high-density ligands and excellent properties, the metal-organic framework (MOF) with high specific surface area and abundant Fe^{3+} binding sites, NH_2-MIL-101(Fe), was synthesized as the main structure of MERT. Moreover, compared to other MOFs (Cu-BTC, MOF-74, and MOF-5), NH_2-MIL-101(Fe) possesses better stability in aqueous solutions, which can withstand continuous capture-washing-elution process for the further practical application[40,41]. Gold nanoparticles (AuNPs) were then grown *in situ* onto the surface of NH_2-MIL-101(Fe) to form MOF@AuNPs *via* electrostatic interactions of positively charged $[NH_4]^+$ with $[AuCl_4]^-$ (Scheme 1). To enhance their specificity, target binding capacity, and anti-fouling ability, MOF@AuNPs were functionalized with a mass of CDR-specific ligands (HH24) and non-CDR-specific ligands (CH1S-6T). Commonly, the HH24 peptide was immobilized onto the NH_2-MIL-101(Fe) surface *via* metal chelation interactions between its His-tag and Fe^{3+} ions in MOF, while the CH1S-6T aptamer with sulfhydryl group was immobilized by Au-S bond on the surface of AuNPs. In addition, the short peptide HS12 (its polyhistidine tag can effectively shield the resultant metal ion sites on the material's surfaces) and an oligonucleotide sequence poly A (it has a strong anti-fouling ability on Au surfaces comparable to Au-S chemical bonds) were successively immobilized on the surface of MOF@Au@HH24@CH1S-6T to prevent the non-specific interferences of residual Fe^{3+} and Au sites[30,31]. Finally, MOF@Au@HH24 and MOF@Au@CH1S-6T were synthesized using a similar method for comparison studies.

The morphologies of NH_2-MIL-101(Fe) and MOF@AuNPs were observed by scanning electron microscope (SEM), energy dispersive spectrometer (EDS), and transmission electron microscope (TEM). As shown in Fig. 1a–c, the sizes of the obtained NH_2-MIL-101(Fe) and the AuNPs grown on its surface were about 300–500 nm and 10–20 nm, respectively. EDS mapping results (Fig. 1d–i) prove the distribution of the different elements (C, N, O, Fe, Au) in MOF@AuNPs. Fig. 1j further shows the XRD patterns of NH_2-MIL-101(Fe) and MOF@AuNPs. Major peaks were present at thetas of 9.45 and 10.13, which can be attributed to NH_2-MIL-101(Fe), while peaks at thetas of 37.15, 43.97, 64.12, and 77.51, can be assigned to the characteristic peaks of AuNPs. The XPS spectra (Fig. 1k) also confirmed that MOF@AuNPs contained C, N, O, Fe, and Au elements. The above results well demonstrated the successful growth of AuNPs onto NH_2-MIL-101(Fe). As illustrated by zeta-potential analysis (Fig. 1l), the surface charge of NH_2-MIL-101(Fe) was changed from positive to negative after the *in-situ* growth of AuNPs. Then the functionalization of MOF@AuNPs with the electrically neutral HH24 (pI $\approx$ 6.57) reduced the surface electronegativity of the obtained material. However, the subsequent anchoring of the negatively charged CH1S-6T on the Au surface increased the electronegativity of the resultant material. Those changes in zeta potential proved the effective immobilization of affinity ligands on the MOF@AuNPs. Fourier transform infrared spectroscopy (FT-IR) spectra were taken to further evaluate whether these ligands were anchored on the surface of MOF@AuNPs. As shown in Fig. 1m, after modification of MOF@AuNPs with HH24, the peaks at 1577 and 1680 cm^{-1} were enhanced (curve iv *vs* curve ii), which may be caused by the carboxylate and amide groups of the immobilized peptide. After further functionalization of MOF@Au@HH24 with CH1S-6T, the characteristic peaks at 2931 and 2847 cm^{-1} have sprung up (curves iii and v) and can be assigned to the vibration of $-CH_3$ in the aptamer, while peaks at 1154 and 1059 cm^{-1} can be attributed to the phosphate radical in

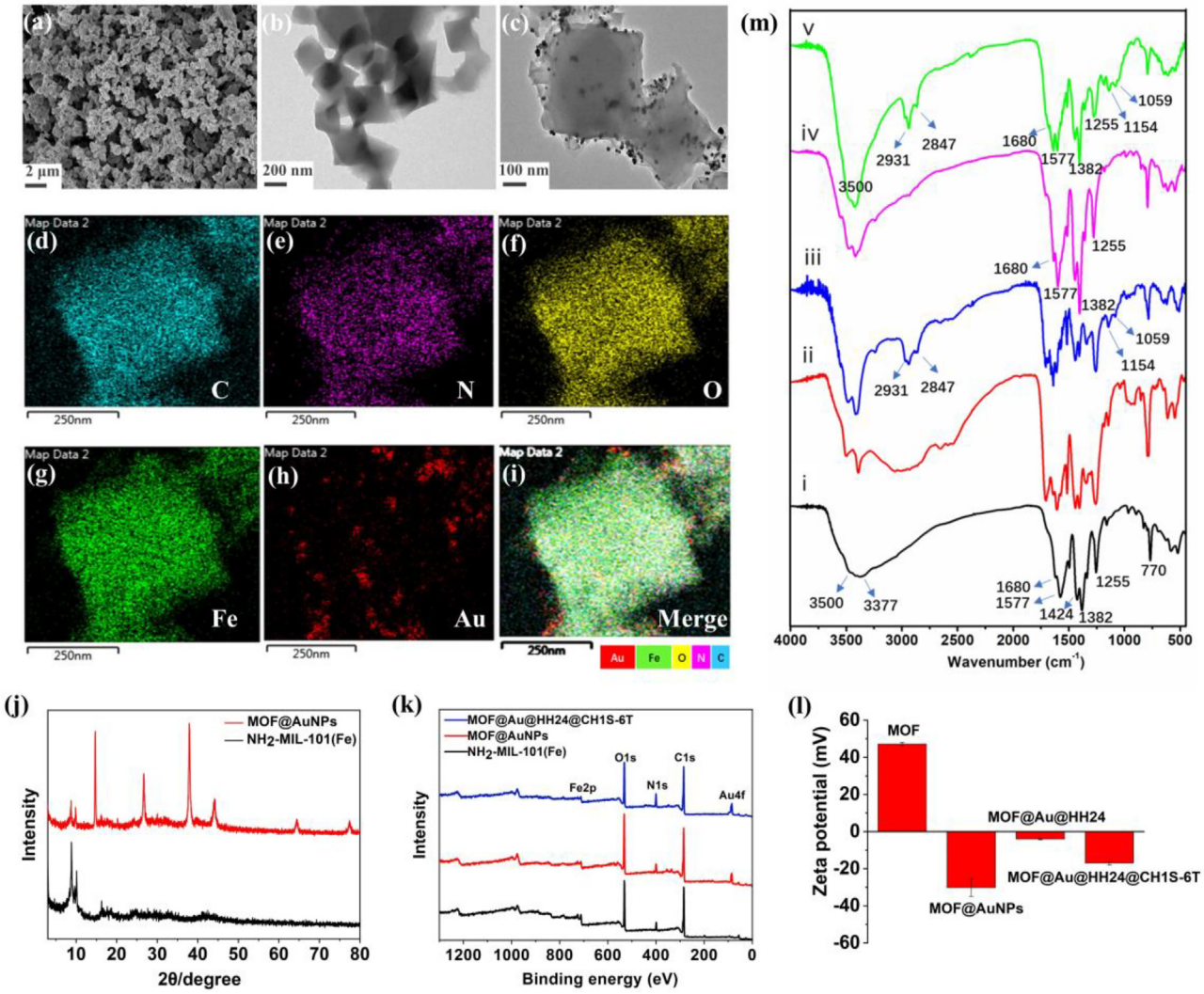

Figure 1 (a) SEM and (b) TEM observations of NH_2-MIL-101(Fe). (c) TEM and (d)−(i) EDS mapping results of MOF@AuNPs. (j) XRD patterns of NH_2-MIL-101(Fe) and MOF@AuNPs. (k) XPS spectra of NH_2-MIL-101(Fe), MOF@AuNPs, and MOF@Au@HH24@CH1S-6T. (l) Zeta potentials of MOF, MOF@AuNPs, MOF@Au@HH24, and MOF@Au@HH24@CH1S-6T. (m) FT-IR spectra of (i) NH_2-MIL-101(Fe), (ii) MOF@AuNPs, (iii) MOF@Au@CH1S-6T, (iv) MOF@Au@HH24, (v) MOF@Au@HH24@CH1S-6T.

the aptamer. Moreover, benefitting from the abundant Fe^{3+} and Au binding sites of MOF@AuNPs, superior ligand densities for HH24 (about 425.8 mg/g material), and CH1S-6T (about 0.86 μmol/g material) were achieved. Therefore, the MOF@Au@HH24@CH1S-6T with excellent properties and ligand densities was successfully fabricated for further applications.

2.2. Comparative studies of the multiepitope recognition material with the mono-epitope affinity materials and other previously reported materials

Trastuzumab is the main antibody unit of anti-HER2 ADCs (commercial Kadcyla, Enhertu, and candidate BAT8001), so it can be selected as an initial model protein for the optimization of recognition conditions. After optimization of the recognition conditions (Supporting Information Fig. S1 and Section S2.1), a comparison between MOF@Au@HH24@CH1S-6T, MOF@Au@HH24, and MOF@Au@CH1S-6T was performed to evaluate the superiority of the multiepitope recognition material. Firstly, the binding capacities of these materials for trastuzumab were compared by evaluating their binding isotherms and kinetic binding (Fig. 2a and b). According to the Langmuir formula, the maximum binding capacity (Q_m) of MOF@Au@HH24 was 648.4 mg/g of material, that of MOF@Au@CH1S-6T was 455.2 mg/g, while that of MOF@Au@HH24@CH1S-6T was 1216.7 mg/g. The kinetic binding curves also indicated that the saturated dynamic binding capacity (Q_e) derived from the pseudo-second-order kinetics equation was calculated to be 913.9 mg/g for MOF@Au@HH24, 406.0 mg/g for MOF@Au@CH1S-6T, and 1438.0 mg/g for MOF@Au@HH24@CH1S-6T, respectively. These results demonstrated that the binding capacity of MERT is

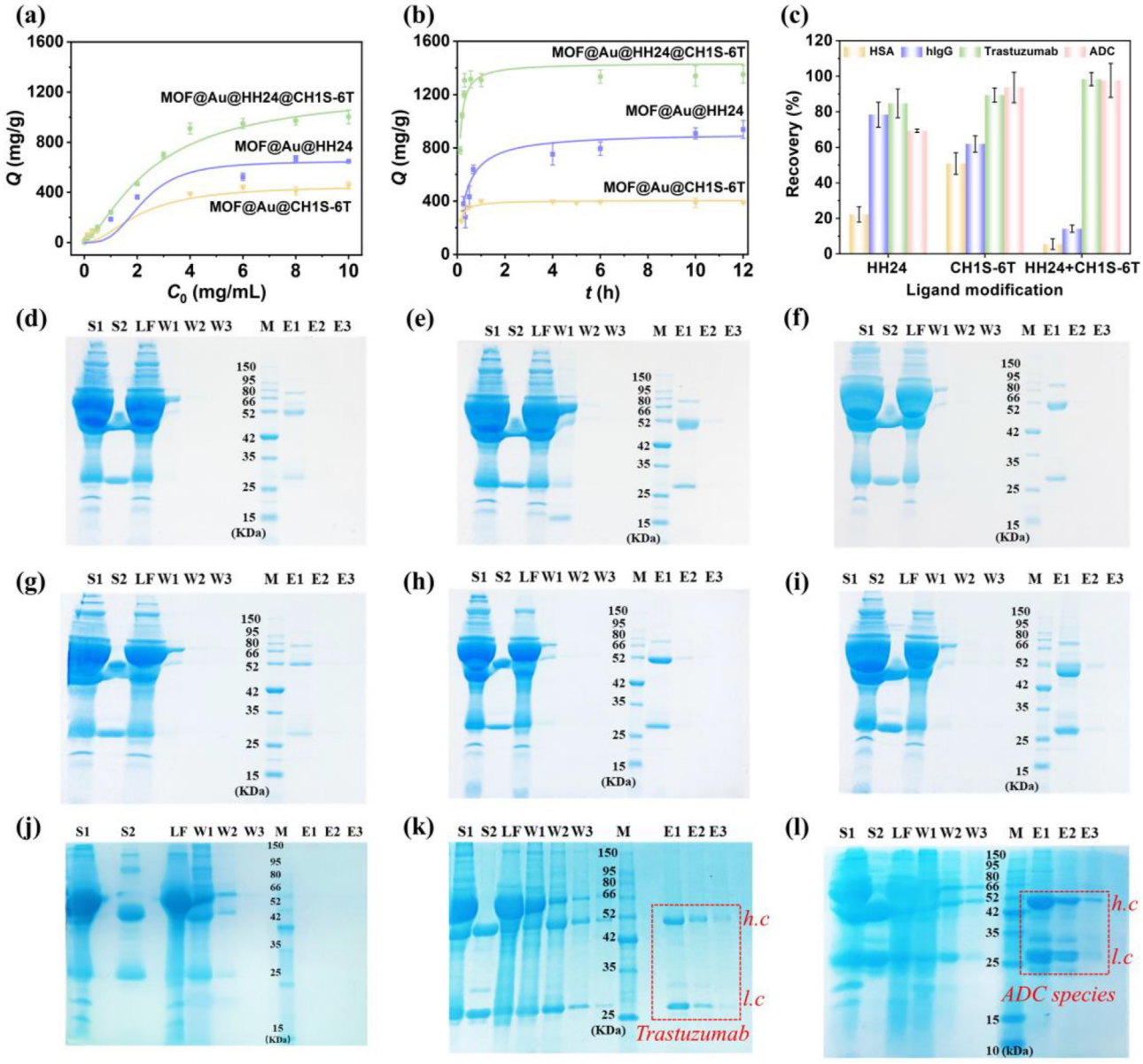

Figure 2 (a) Adsorption isotherms and (b) kinetic binding of the MOF@Au@HH24@CH1S-6T, MOF@Au@HH24, and MOF@Au@CH1S-6T for trastuzumab. (c) Recovery of standard samples purified with different materials. Application of MOF@Au@HH24 to the purification of (d) 10-fold diluted blank human serum, (e) trastuzumab, and (f) ADC spiked into 10-fold diluted human serum. Application of MOF@Au@CH1S-6T to the purification of (g) 10-fold diluted blank human serum, (h) trastuzumab, and (i) ADC spiked 10-fold diluted human serum. Application of MOF@Au@HH24@CH1S-6T to the purification of (j) 10-fold diluted blank human serum, (k) trastuzumab, and (l) ADC spiked 10-fold diluted human serum. LF: loading fractions, WF: washing factions, EF: elution fractions, M: marker. S1 in (d), (g), and (j): 10-fold diluted human serums; S1 in (e), (h), and (k): trastuzumab spiked 10-fold diluted human serums; S1 in (f), (i), and (l): ADC spiked 10-fold diluted human serums. S2 in (d), (e), (g), (h), (j), and (k): trastuzumab; S2 in (f), (i), and (l): ADC.

not only much higher than that of mono-epitope recognition materials, but also ten or even hundreds of times higher than that of previously reported materials for antibody enrichment based on fragment crystallizable (Fc)-specific ligands (such as Protein A, L-histidine, or Fc-affinity peptide) (Supporting Information Fig. S2a)[34,42–46]. In particular, compared to an affinity material for trastuzumab enrichment such as the Tra19 peptide immobilized membrane (ligand density = 5.1 ± 1.3 mg/mL; Q_{max} = 1.3 ± 0.3 mg/mL)[34], MERT shows superior ligand density and binding capacity for trastuzumab.

Subsequently, different proteins, including HSA, hIgG, trastuzumab, and anti-HER2 ADC, were successively employed as analytes to evaluate the enrichment performances and anti-interference abilities of different materials. As depicted in Fig. 2c, these comparative studies indicated that the MOF@Au@HH24@CH1S-6T possessed optimal selectivity and the highest binding recovery towards trastuzumab (98.4%) and even anti-HER2 ADC (97.7%), better than that of MOF@Au@HH24 (69.3% for ADC) or that of MOF@Au@CH1S-6T (93.7% for ADC). Besides, 10 times

diluted blank serum was used to monitor the anti-interference ability of the materials. According to the related SDS-PAGE results, compared to the MOF@Au@HH24@CH1S-6T (Fig. 2j), the MOF@Au@HH24 (Fig. 2d) and MOF@Au@CH1S-6T (Fig. 2g) showed non-specific adsorption from serum, especially due to high homology hIgG and high abundance HSA. Owing to these defects of mono-epitope affinity technology, more sophisticated analytical methods are requested to avoid interferences when analyzing mAbs or ADCs in serum/plasma samples[47−49]. Those procedures undoubtedly increase time consumption and may introduce artifactual modifications or loss of key targets[50−52]. Fortunately, MERT's superior selectivity and anti-interference ability can facilitate efficient enrichment and in-depth analysis of ADCs in serum. As depicted in Fig. 2k and l, most of the interfering components were removed with the washing buffer and appeared in the loading and washing fractions, only trastuzumab or anti-HER2 ADC could be successfully captured from the spiked serum and then eluted with the elution buffer. All the above results confirmed that the novel MERT approach based on MOF@Au@HH24@CH1S-6T possesses excellent antibody binding capacity, specificity, and anti-interference ability. These excellent performances may come from the following assumptions: (1) MOF@AuNPs can provide abundant active sites to accommodate more ligands, which may increase the probability of target-specific binding; (2) in theory, the MERT material can simultaneously bind to different key regions of the target ADC. The potential synergistic binding effects of the two ligands could enhance their binding ability and specificity towards the target ADC, and thus overcome the recognition deficiencies of traditional affinity materials; (3) the rich ligand modification on the surface of MOF@AuNPs could form steric barriers to effectively reduce the interference from biological matrix components.

Finally, the underlying reasons for the excellent performances of MOF@Au@HH24@CH1S-6T were investigated. MST results indicated that the K_d value between HH24 and trastuzumab was 26.4 μmol/L, while the K_d value between CH1S-6T and trastuzumab was determined to be 50.8 nmol/L (Fig. S2b)[33]. In particular, we have studied the molecular interactions in the HH24-ADC-CH1S-6T ternary complex in detail. The anti-HER2 ADC with the most common form was utilized as the classic model to perform molecular docking (Fig. 3a and b), followed by all-atom, explicit water molecular dynamics (MD) simulations (Supporting Information Figs. S3−S5). As shown in Fig. 3c and d, molecular docking and simulation analysis demonstrated that CH1S-6T and HH24 could effectively bind to the ADC in two ways: by binding to the Fab regions on the same side (mode 1, Fig. 3c) or on different sides of the ADC (mode 2, Fig. 3d). According to the root mean square deviation (RMSD) results, the ternary complex has achieved equilibrium after 100 ns (Fig. 3e), and the flexibility of amino acid or nucleotide residues in HH24 and CH1S-6T was also confirmed by the related root mean square fluctuation (RMSF) values (Fig. 3f and g, Supporting Information Table S1). In mode 1 (Fig. 3c), CH1S-6T binds to the light chain of the ADC through hydrogen bonds and salt bridges, involving residues Ser10, Lys107, Lys145, Gln147, Gly157, Asn158, Ser159, and Glu161 of the light chain. And HH24 could bind to the heavy chain and the light chain of the ADC *via* hydrogen bonds, salt bridges, and $\pi-\pi$ stacking interactions, involving residues Tyr33, Arg50, Trp99, and Tyr105 of the heavy chain and Ser50, His91, Tyr92, Thr93, and Thr94 of the light chain. In mode 2 (Fig. 3d), CH1S-6T is still bound to the light chain of the ADC through hydrogen bonds and salt bridges, but the residues involved are Ser10, Arg18, Thr20, Lys103, Lys107, and Lys145 on one light chain. For its part, HH24 is bound to the heavy chain and the light chain on another side of the ADC through hydrogen bonds and salt bridges, involving residues Arg50, Arg59, and Asp102 of the heavy chain and Arg66, His91, Tyr92, Thr93, and Thr94 of the light chain. It is worth noting that HH24 binds with residues located in the CDR region, while CH1S-6T binds between the light chain variable region and the constant region (non-CDR region) of the ADC. The total binding energies (ΔG_{total}) for HH24 with the ADC in the two modes were measured to be -29.02 ± 6.25 and -19.95 ± 5.91 kcal/mol, while those of CH1S-6T with the ADC were -49.73 ± 8.16 and -30.17 ± 7.25 kcal/mol, respectively (Fig. 3h and Supporting Information Tables S2−S5). This suggests that HH24 and CH1S-6T could spontaneously form a tight and stable ternary complex with the ADC in both modes, and these binding regions are spatially separated and do not interfere with each other. Compared with the limited recognition site and binding mode of mono-epitope recognition technology, HH24 and CH1S-6T in MERT could tightly bind to different key sites in the CDR and non-CDR regions of the ADC. When key sites on the ADC are mutated or modified by drugs, the MERT material could still efficiently capture the ADC with flexible recognition modes, thus it has great potential to establish a reliable bioanalytical platform by combination with LC−MS for ADC analysis in complex biological samples.

2.3. Development and verification of the bioanalytical platform based on MERT

Benefitting from the high specificity, target binding capacity, and comprehensive ability of the MOF@Au@HH24@CH1S-6T, a novel bioanalytical platform for ADC subunit evaluation was then developed by combining highly efficient RPLC−QTOF-MS with MERT. For subunit analysis, the model cysteine-linked anti-HER2 ADC was firstly reduced by dithiothreitol (DTT)/tris(2-carboxyethyl)phosphine (TCEP) to produce six fragments (Supporting Information Fig. S6a): light chain (Lc) without drug (Lc0), Lc with 1 drug (Lc1), heavy chain (Hc) without drug (Hc0), and Hc with 1−3 drugs (Hc1−3, respectively). To ensure the application potential of this bioanalytical platform, some key parameters (including elution buffer composition, LC−MS conditions, antibody reduction agent, and conditions) were systematically optimized. Firstly, considering that the above acidic elution buffer B1 contains a small amount of salts and surfactant (Tween-20), the enriched ADC should be treated by ultrafiltration or even dialysis before reduction or injection, which may cause target loss and increase the pretreatment time. Therefore, a comparison between buffer B1 and buffer B2 [(0.1% formic acid (FA), 25% acetonitrile (ACN)] was performed. Good enrichment performances and better ADC subunit peak shapes were achieved using buffer B2 (Fig. S6b−S6e). Thus, buffer B2 (0.1% FA, 25% ACN) was selected as elution buffer for ADC enrichment and analysis. Subsequently, some LC−MS conditions, such as the UV detection wavelength (214 nm), the optimum sample loading (4−16 μg), and the TCEP reduction conditions (50 °C, 30 min) were optimized, as reported in Supporting Information Section 2.2 (Supporting Information Figs. S7−S11, Tables S6−S7).

Finally, a more complex sample, ADC spiked into 3-fold diluted serum, was used to investigate the feasibility of the novel bioanalytical platform including the pre-treatment step (Fig. 4a). As shown in Fig. 4b and Supporting Information Fig. S12, ADC

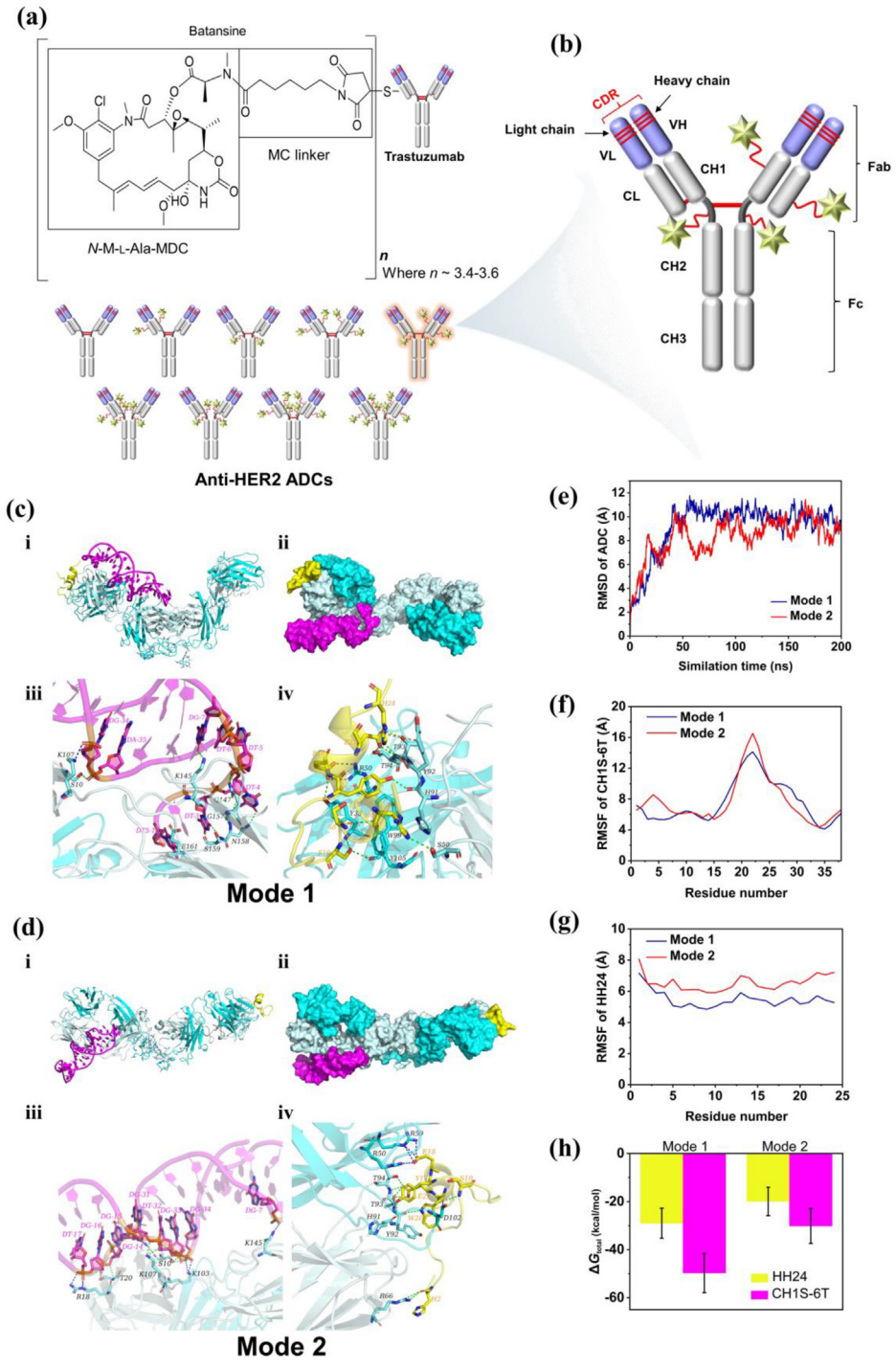

Figure 3 (a) Structure and possible forms of anti-HER2 ADC. (b) ADC with the most common form as the classic model for molecular docking and simulation analysis. Final stable structure of HH24-ADC-CH1S-6T complex in binding modes 1 (c) and 2 (d). (i) and (ii) are the overviews of the complex; (iii) and (iv) show the binding details of CH1S-6T and HH24 to the ADC. The heavy chains and the light chains of the ADC are colored in cyan and pale cyan, respectively. The HH24 is colored in yellow while CH1S-6T is in magenta. The hydrogen bonds and salt bridge interactions in the HH24-ADC-CH1S-6T complex are shown as green and blue dashed lines, respectively. (e) RMSD curve of the ADC in the two binding modes. RMSF of CH1S-6T (f) and HH24 (g) in the two binding modes. (h) Total binding energies for HH24 and CH1S-6T with the ADC in the two binding modes.

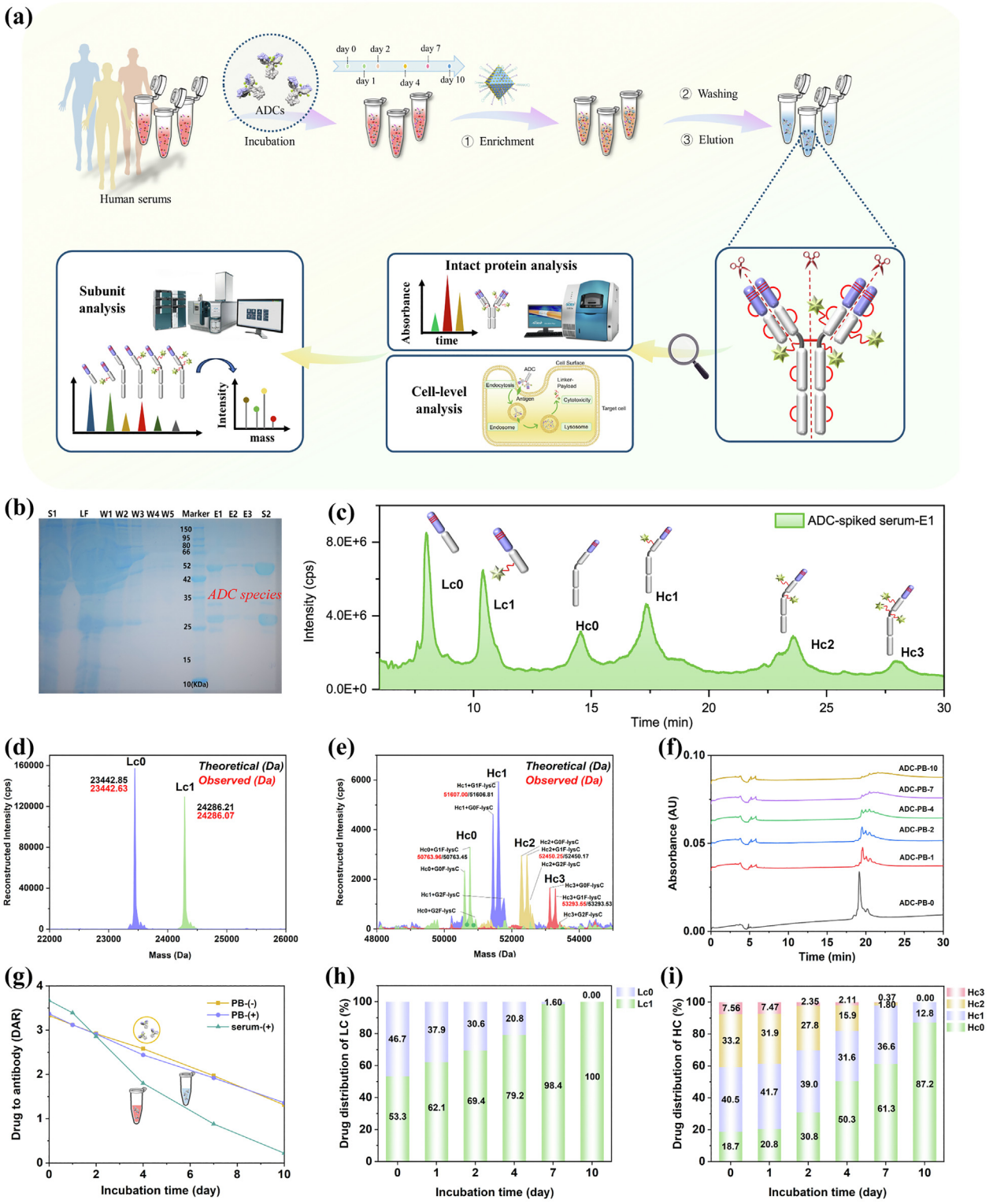

Figure 4 (a) Schematic illustration of MERT combined with LC−QTOF-MS for in-depth analysis of ADCs. (b) Enrichment of ADC from spiked 3-fold diluted serum using MOF@Au@HH24@CH1S-6T. Lanes: S1, feedstock; S2, standard ADC; LF, loading fractions; W, washing fractions; E, elution fractions. LC−QTOF-MS analysis of the eluted fraction 1 (E1), including (c) total ion chromatogram (TIC) image; (d−e): MS deconvolution for light (LC) and heavy (HC) chains. (f) Capillary zone electrophoresis (CZE) direct analysis of standard ADC spiked into PB after incubation (0−10 days, 37 °C). (g) DAR dynamic tracking analysis of ADC in different incubation samples. PB-(−) and PB-(+): before and after ADC enrichment from the spiked incubation PB samples, respectively; serum-(+): after ADC enrichment from the spiked incubation serum samples. DLD analysis for (h) light chains and (i) heavy chains of ADC after enrichment from 3-fold diluted serum.

can be precisely captured from this complex serum sample due to the excellent specificity and anti-interference ability of the multi-epitope recognition material. This performance was further demonstrated by the subunit analysis of the enriched ADC (Fig. 4c–e). In addition, as shown in Supporting Information Fig. S13 and Table S8, the comparison with mono-epitope recognition materials indicated that the elution fraction collected from MOF@Au@HH24 not only had the lowest signal response, but also the calculated DAR was much higher than that of the standard ADC, whereas the elution fractions from MOF@Au@CH1S-6T and MOF@Au@HH24@CH1S-6T gave closer DAR values to that of the standard ADC. Moreover, the elution fraction from the multi-epitope recognition material exhibited a stronger peak response, making it more suitable for the investigation of low-abundant biotransformation variants. Based on the above results, the novel bioanalytical platform based on MERT seems to have great application potential for ADC analysis in complex biological samples.

2.4. *Dynamic DAR and DLD monitoring of the ADC*

Although ADCs are expected to facilitate the targeted delivery of cytotoxic drugs to enhance their tumor-fighting effects and minimize systemic toxicity[52], their efficacy and safety could be compromised because of drug deconjugation on the ADC with time while in circulation, resulting in a dynamic change of DAR[53]. In addition, the DLD (drug load distribution, indicating the fractions of the antibody containing zero, one, two …, *n* drugs) of the ADC is also a crucial characteristic because the different forms could have different toxicological and pharmacological properties[54]. Thus, monitoring the dynamic changes of DAR and DLD will help understand the overall fates of the ADC and provide a theoretical basis for *in vivo* biotransformation study of the ADC.

During the early-stage development of ADC candidates, clinical samples are typically not available; thus, 3-fold diluted human serum samples spiked with the ADC were employed and incubated over an extended period (0, 1, 2, 4, 7, 10 days) to predict the dynamic changes of ADC in the circulation system. Additionally, PB samples spiked with the ADC and 3-fold diluted blank serum samples were incubated and used for comparison. Firstly, the charge variants of the standard ADC in incubated spiked PB samples were monitored by CZE analysis. As can be seen in Fig. 4f, the main peak completely disappeared after only 10 days, and abundant acidic variants were generated. Subsequently, the DAR changes of the ADC in different incubation samples were tracked by analyzing the subunits after enrichment using the MERT approach and TCEP reduction. As shown in Supporting Information Fig. S14a and S14b, all ADC subunits were separated and their peak intensities decreased with the increase of incubation time. Moreover, a similar DAR downtrend was observed for the ADC before [PB-(−)] or after [PB-(+)] enrichment from incubated spiked PB samples (Fig. 4g, Supporting Information Table S9). In particular, the bioactivity changes in incubated spiked PB samples (from 0 to 10 days) were also monitored using antiproliferation assay and cell apoptosis tests. Firstly, the IC_{50} of ADC for HER2+ breast cancer cells (SKBR3 cells) was slightly increased from 8 to 10 ng/mL with the extension of the incubation time (Supporting Information Table S10). Secondly, according to flow cytometry analysis in Fig. 5a, 14.30% of cell apoptosis was induced by the ADC in PB buffer (0 day). However, the effect of cell death induced by the ADC gradually weakened and was even reduced to 7.34%−7.36% after 7−10 days of incubation (Fig. 5a). Finally, the apoptosis-related protein cleaved poly(ADP)-ribose polymerase (PARP) was obviously reduced when SKBR3 cells were treated with the ADC after 10-day incubation (Fig. 5b). These results indicated that the

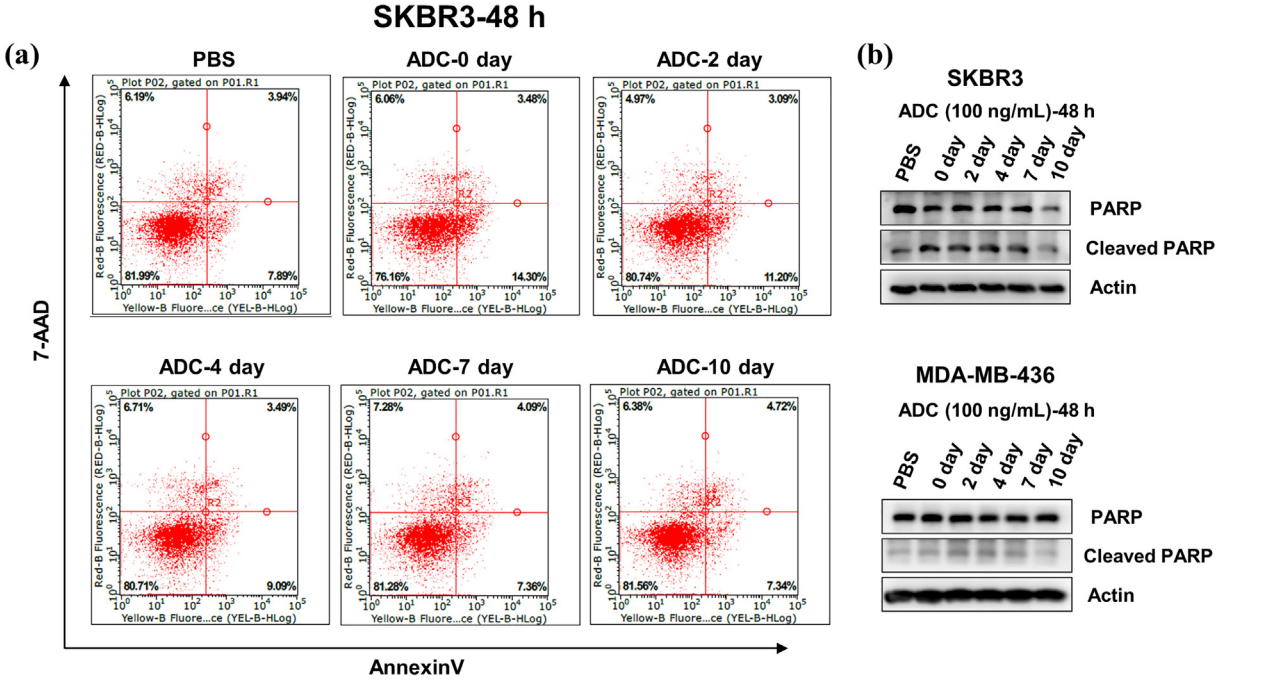

Figure 5 Cell apoptosis induced by the ADC in SKBR3 cells after different incubation times. (a) Cell apoptosis induced by the ADC in SKBR3 cells. (b) Effects of the ADC on the apoptosis-related protein PARP cleavage by Western blot analysis. For the flow cytometry experiment, cells were treated with indicated doses of ADC for 48 h before DNA labeling with 7-amino-actinomycin D (7-AAD) and staining of cell membranes with Annexin V.

reduction of apoptosis ability of the incubated ADC for SKBR3 cells could be attributed to the occurrence of some unexpected issues, such as payload deconjugation or linker cleavage, etc.

The dynamic monitoring of the ADC in spiked human serum samples was subsequently performed. Significantly different trends were observed: (1) According to the chromatographic separation results at the subunit level (Fig. S14c), the chromatographic peaks of heavy chain subunits (Hc1, Hc2, Hc3) of the ADC had almost disappeared after 4-day incubation. (2) A dramatic decrease of DAR was observed from 3.67 (0 day) to 0.22 (10 days), which is obviously faster than that obtained with spiked PB samples (Fig. 4g). (3) DLD analysis revealed the gradual enhancement of subunits Lc0 and Hc0 with the rapid reduction of other drug-carrying species (Lc1, Hc1, Hc2, Hc3). After 10 days, only a small amount of Hc1 was detected by the bioanalytical platform while the other three drug-carrying subunits were completely undetectable (Fig. 4h and i). These dramatic change trends of DAR and DLD further reflected the potential deconjugation of payloads or the unexpected dissociation of linkers.

2.5. *Dynamic tracking analysis of ADC biotransformation in human serum*

ADC biotransformation, such as antibody modifications, protein mass adduct/loss, and payload deconjugation or metabolism, often occur due to the nature of the *in vivo* circulation system, and the instability and complexity of the conjugation sites or linkers[12,16]. Such a biotransformation could potentially decrease ADC efficacy and increase off-target toxicity[5]. Therefore, the study of ADC biotransformation is crucial in helping guide the engineering efforts of ADCs and elucidate the metabolism/catabolism pathways of ADCs *in vivo*.

For the biotransformation analysis of the anti-HER2 ADC in incubated serum, the dynamic changes of light chain subunits (Lc0 and Lc1) were mainly tracked using the proposed bioanalytical platform. After incubation for 7 days, according to the TIC results, a bifurcation peak was observed (Supporting Information Fig. S15), accompanied by the main peak I of Lc0. In particular, the deconvoluted mass spectra (Fig. 6) indicated a difference of 1 Da between the main peak I (Lc0, 23442.2 Da, 7 days, Fig. 6c) and the bifurcation peak (23,443.1 Da, 7 days, Fig. 6d). This could be attributed to the deamidation of asparagine or isomerization of aspartic acid in Lc0 peptide chain because of the complete reduction of the interchain and intrachain disulfide bonds under the optimal TCEP conditions. Based on the *in vivo* modification analysis of trastuzumab an easy deamidation site (asparagine 30 in the light chain) could be responsible for the above event[33]. It is interesting to note that the response intensity of the Lc1 subunit gradually decreased with the extension of incubation time (Fig. 6g−j). Specifically, the emergence of the peak at 24,303.9/24,303.7 Da (new species A1, Fig. 6i−j) confirmed the hydrolysis of the succinimide ring on the MC linker. Moreover, new species at 23,740.6 and 23,757.0 Da were observed. As depicted in Fig. 6, an approximate 546 Da mass decrease (23,740.6 Da for new species B with deamidation or isomerization in Fig. 6d *vs.* 24,285.8 Da for Lc1 in Fig. 6g) and an approximate 547 Da mass decrease (23,757.0 Da for new species B1 in Fig. 6d *vs.* 24,303.9 Da for new species A1 in Fig. 6i) of the related subunits, implying that new catabolites were formed following the loss of maytansinol (m/z = 565 Da) through the ester hydrolysis of the linker-drug. Besides, compared to species B without deamidation or isomerization, the presence of a peak at 23,757.0 Da (new species B1, Fig. 6d) further verified the hydrolysis of the succinimide ring on the linker[55]. All proposed structures and potential biotransformation pathways of the ADC are summarized in Fig. 7. These results indicated that the MERT has good enrichment potential for ADC and its biotransformation variants. Furthermore, the subunit level analysis based on the novel bioanalytical platform can overcome the shortcomings of the intact level analysis. For example, although Orbitrap MS possesses superior mass resolution in comparison to conventional TOF-MS, the mass change resulting from hydrolysis and deamidation/isomerization was too small to be unambiguously resolved for a ~150-kDa molecule[55]. Therefore, the intact level analysis indicated that the non-hydrolyzed molecule was not resolved from the corresponding hydrolyzed version and they merged into one peak[55]. This may suggest that the subunit level analysis could not only detect the modifications of low molecular mass (both for linker-drug and antibodies), but also have less error, more accurate inference, and lower instrumentation requirements in the characterization of ADC and its variants.

These above findings will also be advantageous in predicting the possible biotransformation of ADC *in vivo*, including 1) the ADC undergoes the loss of maytansinol *via* ester hydrolysis; 2) the ADC is subject to a small mass increase over time in biological fluids due to the hydrolysis of the succinimide ring on the MC linker; 3) some key modifications of the antibody could occur, such as asparagine deamidation or aspartic acid isomerization. These findings could also provide some key suggestions or evidence for the next-generation ADC development: (1) the DAR of ADC can be appropriately enhanced to maintain their bioactivity and efficacy, such as DS-8201 (DAR = 7 to 8); (2) a relatively robust linker and a low-toxicity payload with bystander effects could reduce the risk of drug deconjugation; (3) in particular, more efficient and specific site-directed coupling technology was desired to reduce the heterogeneity and potential immune recognition deficiencies of traditional ADCs. In summary, the novel bioanalytical platform based on MERT exhibited a great application perspective for the design and optimization of ADC candidates.

3. Conclusions

ADC bioanalysis is challenging due to serious matrix interferences, high heterogeneity, complex biotransformation of ADCs, and in particular immune recognition deficiencies of traditional affinity technologies. In this work, a MERT approach was developed by simultaneously immobilizing the CDR mimotope peptide HH24 and the non-CDR aptamer CH1S-6T onto the MOF@AuNPs. Compared to traditional affinity technologies, MERT possesses some advantages: firstly, MERT can specifically recognize different key regions of the target ADC. The potential synergistic binding effects of these two ligands could enhance their binding ability and selectivity towards ADCs, and thus overcome the immune recognition deficiencies of traditional affinity materials. Secondly, the ultrahigh ligand densities (HH24: 425.8 mg/g, CH1S-6T: 0.86 μmol/g), and excellent binding ability of MERT (1438.0 mg/g for trastuzumab) is ten or even hundreds of times higher than that of the mono-epitope or Fc-specific affinity materials. So, MERT can precisely capture the target ADC from human serum containing high homology IgGs. Thirdly, a versatile bioanalytical platform was successfully developed by combining MERT and RPLC−QTOF-MS. Some important dynamic modifications of the ADC, such as the fast changes in DAR and DLD,

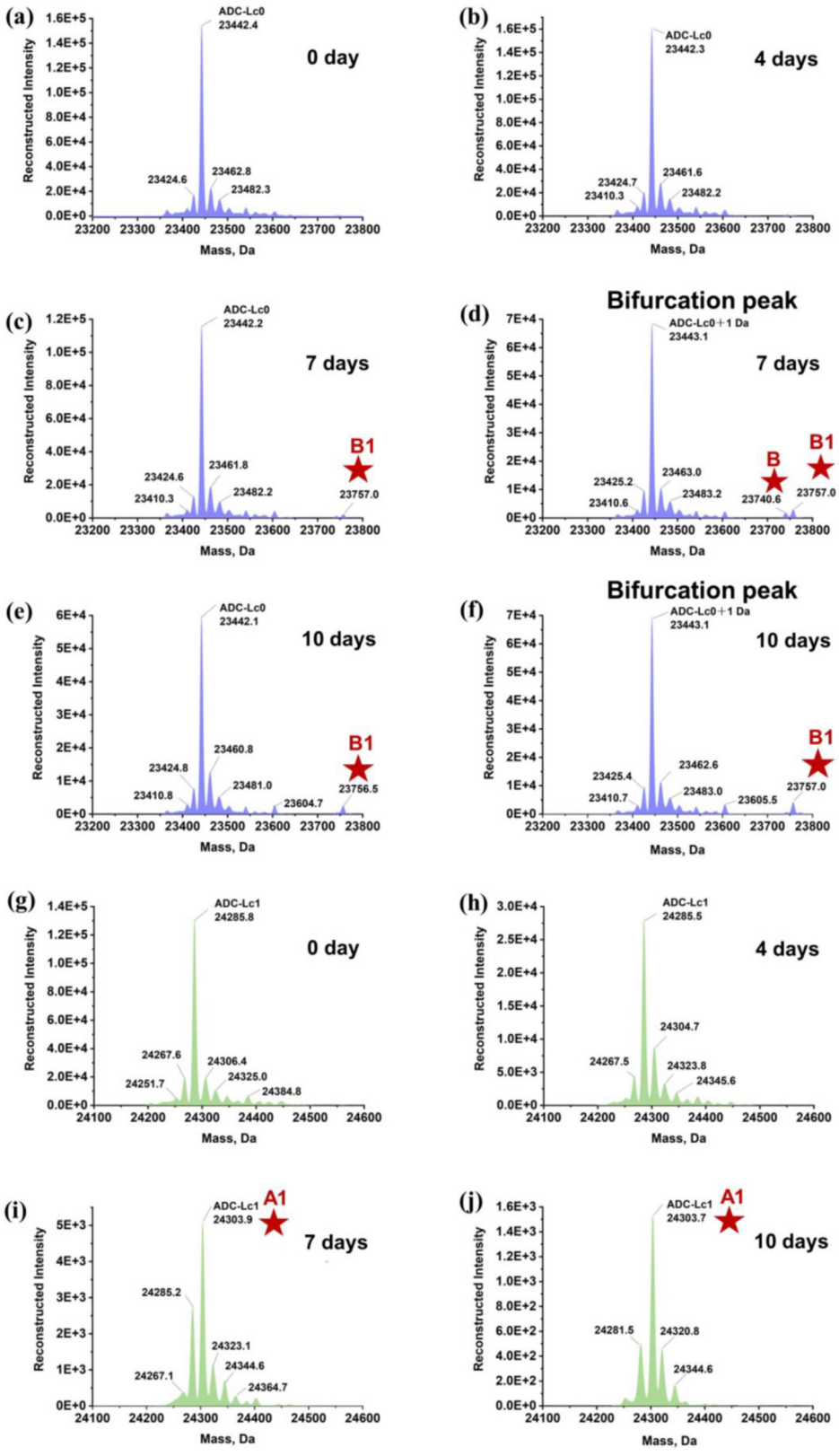

Figure 6 Lc0 and Lc1 deconvoluted mass spectra of the ADC enriched from 3-fold diluted spiked human serum using MOF@Au@HH24@CH1S-6T (incubation time: from 0 to 10 days).

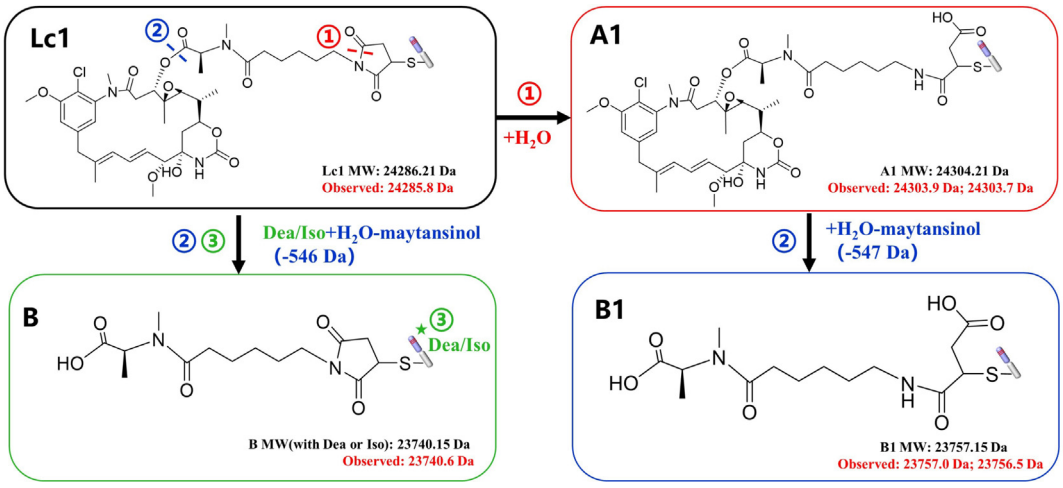

Figure 7 Proposed structures and potential biotransformation pathways of ADC light chain species.

the loss of payloads (maytansinol), the unexpected hydrolysis of the succinimide ring of the linker, and the potential antibody modifications, were monitored using this novel platform. This should serve as a powerful early-stage analytical tool that would greatly reduce the time and cost spent on *in vivo* assays, and the obtained information could inspire the future design of the conjugation chemistry for these biotherapeutics. In a word, the bioanalytical platform based on MERT opens new avenues for the bioanalysis of next-generation ADCs and should then accelerate ADC development.

4. Experimental

4.1. Materials and instrumentation

The BAT8001, an anti-human epidermal growth factor receptor 2 (anti-HER2) ADC, is composed of a trastuzumab biosimilar product (BAT0606) that covalently binds to a drug-linker, *i.e.*, batansine (a derivative of maytansine linked to an uncleavable linker by a stable amide bond). Anti-HER2 ADC (BAT8001) was gifted from Bio-Thera Solutions, Ltd. (Guangzhou, China). Trastuzumab was purchased from China Roche (Shanghai, China). Human immunoglobulin G (hIgG >95%), human serum albumin (HSA≥ 99%) were purchased from Sigma−Aldrich (Shanghai, China). HH24 peptide (HHHHHHGSGSGSQLGPYELWELSH) and HS12 (HHHHHHGSGSGS) peptide were obtained from GenScript Biotechnology, Co, Ltd. (Nanjing, China). CH1S-6T aptamer (TTTTTTGTGTCCAGGGTTCCAAGGTGCTTCGTGGACAC) and polyadenine (poly A) were synthesized by Sangong Bioengineering Co, Ltd. (Shanghai, China). MS-grade water and acetonitrile (ACN) were purchased from Fisher Scientific (Fair Lawn, NJ, USA). Formic acid (FA), 2-amino-2(hydroxymethyl)-1-3-propane diol hydrochloride (Tris-HCl), dithiothreitol (DTT) were purchased from Sigma−Aldrich (St. Louis, MO, USA). Dimethyl formamide (DMF, AR), 2-amino terephthalic acid (98%), ferric chloride trihydrate (AR), chloroauric acid hydrated (≥99.9%), sodium citrate (AR), isopropanol (IPA, 98%), monosodium phosphate (NaH_2PO_4, 98%), disodium hydrogen phosphate (Na_2HPO_4, 98%), sodium chloride (NaCl, 98%), sodium formate (HCOONa, 98%), sodium hydroxide (NaOH, 98%), hydrochloric acid (HCl, 98%), ε-aminocaproic acid (EACA), triethylene tetramine (TETA), and hydroxypropyl methyl cellulose (HPMC) were obtained from Aladdin (Shanghai, China). Phosphate buffer solutions (PBS) (unless otherwise specified, 10 mmol/L and pH 7.4) were bought from Solarbio Science & Technology Co., Ltd. (Beijing, China). Tris(2-carboxyethyl)phosphine hydrochloride [0.5 mol/L TCEP (pH7.0, for mass spectrometry)]), BCA assay kit, and SDS-PAGE kit were obtained from Beyotime Biotechnology Co., Ltd. (Shanghai, China). Water was purified in-house with an ultrapure water polishing system (Omni-A, RO-DI, Xiamen, China). Human serum was provided by the First Affiliated Hospital of Jinan University (Guangzhou, China).

Transmission electron microscope (TEM) and energy-dispersive X-ray spectroscopy (EDS) observations were conducted using a Tecnai G2 Spirit TWIN TEM (FEI, Hillsboro, OR, USA) with a Bruker XFlash 6130 energy dispersive X-ray microanalyzer (Berlin, Germany). Scanning electron microscope (SEM) observations were performed by ZEISS Gemini ultra-55 SEM (Oberkochen, Germany). Fourier Transform Infrared Spectroscopy (FT-IR) spectra were recorded on a Thermo Nicolet iS50 FT-IR Spectrometer (Waltham, MA, USA) with wavenumber range from 4000 to 400 cm^{-1}.

4.2. Synthesis of NH_2-MIL-101(Fe) and MOF@AuNPs

NH_2-MIL-101(Fe) was fabricated by a classical hydrothermal method[56]. Firstly, 0.675 g (2.497 mmol) $FeCl_3 \cdot 6H_2O$ was dissolved in 7.5 mL DMF to get solution A, and 0.225 g (1.242 mmol) NH_2-H_2BDC was dissolved in another 7.5 mL DMF to get solution B. Later, solution A was mixed with solution B for 1 h at room temperature (RT), and the mixture was heated for 24 h at 110 °C in an autoclave. Finally, the product was collected and washed 3 times with DMF and MeOH, respectively, and then dried under vacuum for further use.

MOF@AuNPs were then synthesized by *in-situ* growing of AuNPs on the surface of NH_2-MIL-101(Fe). Briefly, 200 mg NH_2-MIL-101(Fe) were dispersed in 60 mL aqueous solution which contained 0.1% (*w*/*v*) $HAuCl_4 \cdot 4H_2O$ (100 mmol/L). Later, the suspension was stirred continuously for 2.5 h at 45 °C, and then heated to vigorous boiling accompanied by a quick injection of 440 μL of 30% (*w*/*v*) sodium citrate and further stirred for another 40 min at boiling temperature. After cooling to room temperature, the obtained MOF@AuNPs was washed several times with

deionized water. Finally, the product was collected after centrifugation and redispersed into 1 mL deionized water for further use.

4.3. Preparation of MOF@Au@HH24@CH1S-6T

The HH24 peptide was immobilized onto the surface of MOF@AuNPs *via* metal-chelation interaction between Fe^{3+} ions and the His-tag of the peptide. Firstly, the HH24 peptide (2 mg/mL, 1 mL) was incubated with 0.2 mL of MOF@AuNPs suspension. The mixture was incubated at room temperature (RT) for the night, and then washed with deionized water. Subsequently, to block residual metal ion sites on the MOF, 1 mL HS12 (1 mg/mL) was added into the suspension and incubated at RT for another 3 h. After washing with deionized water, the MOF@Au@HH24 was successfully prepared and then redispersed into 0.2 mL deionized water for further use.

To fabricate MOF@Au@HH24@CH1S-6T, the CH1S-6T aptamer with sulfhydryl group was then immobilized on the surface of AuNPs. After annealing, 2 OD TECP-treated CH1S-6T (dissolved in 0.5 mL of deionized water) was incubated with MOF@Au@HH24 at −20 °C for 2 h and 4 °C for 1 h, and then washed with deionized water. Later, 2 OD poly A blocker (dissolved in 0.5 mL of deionized water) was added into the mixture and incubated at 4 °C for 2 h to block the residual active sites on the AuNPs. Ultimately, the excess of poly A was removed from the suspension by centrifugation 3 times at 4500 rpm for 5 min, and the precipitates were redispersed into deionized water to a final concentration of 25 mg/mL. The fabricated MOF@Au@HH24@CH1S-6T was stored at 4 °C for further use.

The ligand density was tested and calculated based on the change of fluorescence intensity of the ligands in the supernatant before and after ligand immobilization. The fluorescence of HH24 is generated by endogenous Trp and Tyr, while the fluorescence of the aptamer is exogenous fluorescence produced by reaction with fluorescein isothiocyanate (FITC).

4.4. Capture of trastuzumab or ADC from complex biological fluids

All experiments involving human serum samples are performed in compliance with the relevant laws and institutional guidelines and have been approved by the ethical committee of Jinan University, China. Diluted human serum spiked with 1 mg/mL solution of trastuzumab or ADC was used as biological sample to measure the purification performance of MOF@Au@HH24@CH1S-6T. After mixing 0.05 mL of MOF@Au@HH24@CH1S-6T with 0.2 mL of each sample, 1 mL of washing buffer (10 mmol/L Tris-HCl, pH 7.0) was used to remove interferences and then 1 mL of elution buffer B1 (10 mmol/L HCOONa, 100 mmol/L NaCl, 0.5% Tween-20, pH 3.25) or 0.6 mL of elution buffer B2 (0.1% FA, 25% ACN) was used to obtain the enriched antibody or ADC. Moreover, diluted blank human serum was used to evaluate the anti-fouling ability of MOF@Au@HH24@CH1S-6T. All fractions were collected for SDS-PAGE analysis or LC−QTOF-MS analysis.

4.5. CZE analysis

The CZE analysis was performed on a Beckman Coulter PA 800 plus capillary electrophoresis system (Brea, CA, USA) equipped with a UV/PDA detector. The capillary (50 μm i.d., total length: 65 cm) was used for all analyses and detection was performed at 214 nm. New capillaries were flushed with sodium hydroxide (1 mol/L), hydrochloric acid (1 mol/L), water, and running buffer consist of 0.1% HPMC, 360 mmol/L EACA, and 1.8 mmol/L TETA, pH 5.7. Before each sample injection, the capillary was rinsed with hydrochloric acid, water, running buffer, then incubated PB samples spiked with the ADC were injected at 2 psi for 30 s. Separations were performed using a voltage of 28 kV. Specific parameters about capillary pretreatment and separation methods are depicted in Supporting Information Tables S11 and S12.

4.6. Tracking analysis of drug-to-antibody ratio (DAR), drug load distribution (DLD), and biotransformation changes of ADC in complex biological fluids

For subunit analysis of the enriched ADC from the incubated samples, the ADC was firstly reduced with 10 mmol/L TCEP at 50 °C for 30 min. Chromatographic separation of the obtained ADC subunits was performed on an Ultimate 3000 UPLC system equipped with BioResolve™ RP mAb polyphenyl column (2.7 μm, 450 Å, 100 mm × 2.1 mm i.d., Waters, Milford, MA, USA). Twenty μL of the ADC subunits were loaded onto the column and then separated with a gradient consisting of mobile phase A (MPA, 0.1% formic acid in water) and mobile phase B (MPB, 0.1% formic acid in ACN), delivered at 60 °C at a flow rate of 0.3 mL/min. The gradient started with a 3-min hold at 10% MPB and then MPB was increased to 30% at 4 min, up to 36% at 30 min, reaching 80% at 31 min and remaining at that level for 0.5 min. Finally, the column was equilibrated again at 10% MPB with a hold from 32 to 35 min.

The ADC subunits were also monitored using SCIEX X500R QTOF mass spectrometer (TurbolonSpray™, AB Sciex, Concord, ON, Canada) coupled to an ExionLC AD system. For the enriched ADC from incubated samples, the same LC conditions were used, while different LC conditions were used for native incubated PB samples: 28% MPB at 4 min, up to 35% MPB at 30 min, all the other parameters being the same. Specific MS parameters for ADC subunit analysis are given in Supporting Information Table S13. TOF-MS spectra were extracted from the total ion chromatograms (TICs) and then deconvoluted using the Bayesian Protein Reconstruct algorithm incorporated in BioPharmaView™ 2.0 software (AB Sciex, Concord, ON, Canada), whose specific parameter setting can be seen in Supporting Information Tables S14 and S15. To analyze the DLD, the number of linkers attached to the light and heavy chains after reduction can be obtained directly from the deconvoluted MS spectra and the peak areas were used to calculate the proportion of the different drug loads. The average DAR was calculated based on the peak areas of the different subunits obtained by LC−QTOF-MS and RPLC−UV, according to Eq. (1)[56,57]:

$$\mathrm{DAR_{av}} = 2 \times \left\{ \left[\sum_{n=0}^{1} (n\mathrm{LC}_n) \div \sum_{n=0}^{1} (\mathrm{LC}_n) \right] + \left[\sum_{n=0}^{3} (n\mathrm{HC}_n) \div \sum_{n=0}^{3} (\mathrm{HC}_n) \right] \right\} \quad (1)$$

where n is the number of attached linker payloads, LC and HC are the peak areas of light and heavy chains, respectively.

Acknowledgments

This work was supported by the National Natural Science Foundation of China (82373829, 82273893, 82173773), the Natural Science Foundation of Guangdong Province, China (2021A1515220099, 2022A1515011576), the High-End Foreign Experts Project, China (G2021199005L), and the Science and Technology Program of Guangdong Provincial Medical Products Administration, China (2023TDZ11, 2022ZDB04). All experiments involving human serum samples are performed in compliance with the relevant laws and institutional guidelines and have been approved by the ethical committee of Jinan University, China.

Author contributions

Yutian Lei: Writing − original draft, Investigation. Yuan Shen: Writing − original draft, Investigation. Feng Chen: Investigation. Rui He: Investigation. Zhang Zhang: Investigation. Ying Zhou: Investigation. Jin-Chen Yu: Resources. Jacques Crommen: Writing − review & editing. Zhengjin Jiang: Writing − review & editing, Funding acquisition. Qiqin Wang: Writing − review & editing, Funding acquisition.

Conflicts of interest

The authors declare that they have no conflicts of interest.

Appendix A. Supporting information

Supporting information to this article can be found online at https://doi.org/10.1016/j.apsb.2024.06.007.

References

1. Dumontet C, Reichert JM, Senter PD, Lambert JM, Beck A. Antibody−drug conjugates come of age in oncology. *Nat Rev Drug Discov* 2023;**22**:641−61.
2. Tarantino P, Pestana RC, Corti C, Modi S, Bardia A. Antibody−drug conjugates: smart chemotherapy delivery across tumor histologies. *CA Cancer J Clin* 2022;**72**:165−82.
3. Carter PJ, Rajpal A. Designing antibodies as therapeutics. *Cell* 2022;**185**:2789−805.
4. Maecker H, Jonnalagadda V, Bhakta S, Jammalamadaka V, Junutula JR, Maecker H. Exploration of the antibody−drug conjugate clinical landscape. *mAbs* 2023;**15**:2229101.
5. Zhao P, Zhang Y, Li W. Recent advances of antibody drug conjugates for clinical applications. *Acta Pharm Sin B* 2020;**10**:1589−600.
6. Colombo R, Rich JR. The therapeutic window of antibody drug conjugates: a dogma in need of revision. *Cancer Cell* 2022;**40**:1255−63.
7. Beck A, Goetsch L, Dumontet C, Corvaïa N. Strategies and challenges for the next generation of antibody−drug conjugates. *Nat Rev Drug Discov* 2017;**16**:315−37.
8. Fu Z, Li S, Han S, Shi C, Zhang Y. Antibody drug conjugate: the "biological missile" for targeted cancer therapy. *Signal Transduct Target Ther* 2022;**7**:93.
9. Fuentes-Antrás J, Genta S, Vijenthira A, Siu LL. Antibody−drug conjugates: in search of partners of choice. *Trends Cancer* 2023;**9**:339−54.
10. Liu T, Tao Y, Xia X, Zhang Y, Deng R, Wang Y. Analytical tools for antibody e drug conjugates : from *in vitro* to *in vivo*. *TrAC-Trends Anal Chem* 2022;**152**:116621.
11. Walsh SJ, Bargh JD, Dannheim FM, Hanby AR, Seki H, Counsell AJ, et al. Site-selective modification strategies in antibody−drug conjugates. *Chem Soc Rev* 2021;**50**:1305−53.
12. Zhu X, Huo S, Xue C, An B, Qu J. Current LC−MS-based strategies for characterization and quantification of antibody−drug conjugates. *J Pharm Anal* 2020;**10**:209−20.
13. Su Z, Xiao D, Xie F, Liu L, Wang Y, Fan S, et al. Antibody−drug conjugates: recent advances in linker chemistry. *Acta Pharm Sin B* 2021;**11**:3889−907.
14. Huang Y, Mou S, Wang Y, Mu R, Liang M, Rosenbaum AI. Characterization of antibody−drug conjugate pharmacokinetics and *in vivo* biotransformation using quantitative intact LC−HRMS and surrogate analyte LC−MRM. *Anal Chem* 2021;**93**:6135−44.
15. Zhu C, Han H, Chen Z, Shen Y, Zhang Q, Bao C, et al. Tetrapeptide-based mimotope affinity monolith for the enrichment and analysis of anti-HER2 antibody and antibody−drug conjugate. *Anal Chim Acta* 2023;**1246**:340892.
16. Kotapati S, Passmore D, Yamazoe S, Sanku RKK, Cong Q, Poudel YB, et al. Universal affinity capture liquid chromatography−mass spectrometry assay for evaluation of biotransformation of site-specific antibody drug conjugates in preclinical studies. *Anal Chem* 2020;**92**:2065−73.
17. Jashnani A, Kotapati S, Deshpande M, Yamazoe S, Strop P, Rajpal A, et al. Automated and faster affinity capture method for biotransformation assessment of site-specific antibody drug conjugates. *Anal Chem* 2021;**93**:5371−6.
18. Lei Y, Shen Y, Zuo C, Lu L, Crommen J, Wang Q, et al. Emerging affinity ligands and support materials for the enrichment of monoclonal antibodies. *TrAC-Trends Anal Chem* 2022;**157**:116744.
19. Olaleye O, Spanov B, Ford R, Govorukhina N, van de Merbel NC, Bischoff R. Enrichment and liquid chromatography−mass spectrometry analysis of trastuzumab and pertuzumab using affimer reagents. *Anal Chem* 2021;**93**:13597−605.
20. Beck A, Wagner-Rousset E, Ayoub D, Van Dorsselaer A, Sanglier-Cianférani S. Characterization of therapeutic antibodies and related products. *Anal Chem* 2013;**85**:715−36.
21. Mo J, Yan Q, So CK, Soden T, Lewis MJ, Hu P. Understanding the impact of methionine oxidation on the biological functions of IgG1 antibodies using hydrogen/deuterium exchange mass spectrometry. *Anal Chem* 2016;**88**:9495−502.
22. Schadt S, Hauri S, Lopes F, Edelmann MR, Staack RF, Villaseñor R, et al. Minireview are biotransformation studies of therapeutic proteins needed ? Scientific considerations and technical challenges. *Drug Metab Dispos* 2019;**47**:1443−56.
23. Zhang Y, Wu SL, Li Y. Comparative study of profiling post-translational modifications of a circulating antibody drug in human with different capture reagents. *Biologicals* 2017;**45**:93−5.
24. Bults P, Bischo R, Bakker H, Gietema JA, van de Merbel NC. LC−MS/MS-based monitoring of *in vivo* protein biotransformation: quantitative determination of trastuzumab and its deamidation products in human plasma. *Anal Chem* 2016;**88**:1871−7.
25. Yan B, Steen S, Hambly D, Valliere-Douglass J, Vanden Bos T, Smallwood S, et al. Succinimide formation at Asn 55 in the complementarity determining region of a recombinant monoclonal antibody IgG1 heavy chain. *J Pharm Sci* 2009;**98**:3509−21.
26. Huang L, Lu J, Wroblewski VJ, Beals JM, Riggin RM. *In vivo* deamidation characterization of monoclonal antibody by LC/MS/MS. *Anal Chem* 2005;**77**:1432−9.
27. Stephan JP, Chan P, Lee C, Nelson C, Elliott JM, Bechtel C, et al. Anti-CD22-MCC-DM1 and MC-MMAF conjugates: impact of assay format on pharmacokinetic parameters determination. *Bioconjug Chem* 2008;**19**:1673−83.
28. Kaur S, Xu K, Saad OM, Dere RC, Carrasco-Triguero M. Bioanalytical assay strategies for the development of antibody−drug conjugate biotherapeutics. *Bioanalysis* 2013;**5**:201−26.
29. Stephan JP, Kozak KR, Wong WLT. Challenges in developing bioanalytical assays for characterization of antibody−drug conjugates. *Bioanalysis* 2011;**3**:677−700.

30. Huang S, Tang R, Zhang T, Zhao J, Jiang Z, Wang Q. Anti-fouling poly adenine coating combined with highly specific CD20 epitope mimetic peptide for rituximab detection in clinical patients' plasma. *Biosens Bioelectron* 2021;**171**:112678.
31. Huang S, Wang W, Li J, Zhang T, Liang Y, Wang Q, et al. Multi-functional DNA mediated spatially confined assembly for antibody orientation: surpassing sensitivity and accuracy for rituximab detection. *Chem Eng J* 2021;**419**:129613.
32. Van Rosmalen M, Ni Y, Vervoort DFM, Arts R, Ludwig SKJ, Merkx M. Dual-color bioluminescent sensor proteins for therapeutic drug monitoring of antitumor antibodies. *Anal Chem* 2018;**90**:3592−9.
33. Lu L, Liu X, Zuo C, Zhou J, Zhu C, Zhang Z, et al. *In vitro/in vivo* degradation analysis of trastuzumab by combining specific capture on HER2 mimotope peptide modified material and LC−QTOF-MS. *Anal Chim Acta* 2022;**1225**:340199.
34. Tan HY, Yang J, Linnes JC, Welch CJ, Bruening ML. Quantitation of trastuzumab and an antibody to SARS-CoV-2 in minutes using affinity membranes in 96-well plates. *Anal Chem* 2022;**94**:884−91.
35. Yang J, Zhou A, Li M, He Q, Zhou J, Crommen J, et al. Mimotope peptide modified pompon mum-like magnetic microparticles for precise recognition, capture and biotransformation analysis of rituximab in biological fluids. *Acta Pharm Sin B* 2024;**14**:1317−28.
36. Labrijn AF, Janmaat ML, Reichert JM, Parren PWHI. Bispecific antibodies: a mechanistic review of the pipeline. *Nat Rev Drug Discov* 2019;**18**:585−608.
37. Fan G, Wang Z, Hao M, Li J. Bispecific antibodies and their applications. *J Hematol Oncol* 2015;**8**:1−14.
38. Li H, Er Saw P, Song E. Challenges and strategies for next-generation bispecific antibody-based antitumor therapeutics. *Cell Mol Immunol* 2020;**17**:451−61.
39. Yang N, Tang Q, Hu P, Lewis MJ. Use of *in vitro* systems to model *in vivo* degradation of therapeutic monoclonal antibodies. *Anal Chem* 2018;**90**:7896−902.
40. Tong YH, Wu YZ, Xu ZL, Luo LH, Jia R, Xu SJ. Dye sieving and dye/salt separation PEI-based loose nanofiltration membrane modified by NH2-MIL-101(Fe) and polyphenol coating. *Sep Purif Technol* 2023;**327**:124989.
41. Joseph L, Saha M, Kim S, Jun BM, Heo J, Park CM, et al. Removal of Cu^{2+}, Cd^{2+}, and Pb^{2+} from aqueous solution by fabricated MIL-100(Fe) and MIL-101(Cr): experimental and molecular modeling study. *J Environ Chem Eng* 2021;**9**:106663.
42. Yang H, Gurgel PV, Carbonell RG. Purification of human immunoglobulin G *via* Fc-specific small peptide ligand affinity chromatography. *J Chromatogr A* 2009;**1216**:910−8.
43. Xu R, Lu L, Sun L, Liu X, Lei Y, Huang S, et al. Development of histidine-tagged cyclic peptide functionalized monolithic material for the affinity purification of antibodies in biological matrices. *J Chromatogr A* 2021;**1635**:461707.
44. Du Z, Zhang S, Zhou C, Liu M, Li G. L-Histidine functionalized multi-walled carbon nanotubes for on-line affinity separation and purification of immunoglobulin G in serum. *Talanta* 2012;**99**:40−9.
45. Chen K, Zhou J, Shao Z, Liu J, Song J, Wang R, et al. Aptamers as versatile molecular tools for antibody production monitoring and quality control. *J Am Chem Soc* 2020;**142**:12079−86.
46. Sun B, Liu J, Cai P, Wu J, Liu W, Hu H, et al. Aptamer-based sample purification for mass spectrometric quantification of trastuzumab in human serum. *Talanta* 2023;**257**:124349.
47. Yin F, Adhikari D, Sun M, Shane Woolf M, Ma E, Mylott W, et al. Bioanalysis of an antibody drug conjugate (ADC) PYX-201 in human plasma using a hybrid immunoaffinity LC−MS/MS approach. *J Chromatogr B Analyt Technol Biomed Life Sci* 2023;**1223**:123715.
48. Suh M jin, Powers JB, Daniels CM, Wu Y. Enhanced pharmacokinetic bioanalysis of antibody−drug conjugates using hybrid immunoaffinity capture and microflow LC−MS/MS. *AAPS J* 2023;**25**:68.
49. Dong L, Li C, Locuson C, Chen S, Qian MG. A two-step immunocapture LC/MS/MS assay for plasma stability and payload migration assessment of cysteine-maleimide-based antibody drug conjugates. *Anal Chem* 2018;**90**:5989−94.
50. Krokhin OV, Antonovici M, Ens W, Wilkins JA, Standing KG. Deamidation of -Asn-Gly- sequences during sample preparation for proteomics: consequences for MALDI and HPLC−MALDI analysis. *Anal Chem* 2006;**78**:6645−50.
51. Du Y, Wang F, May K, Xu W, Liu H. Determination of deamidation artifacts introduced by sample preparation using ^{18}O-labeling and tandem mass spectrometry analysis. *Anal Chem* 2012;**84**:6355−60.
52. Padoan A, D'Incà R, Scapellato ML, De Bastiani R, Caccaro R, Mescoli C, et al. Improving IBD diagnosis and monitoring by understanding preanalytical, analytical and biological fecal calprotectin variability. *Clin Chem Lab Med* 2018;**56**:1926−35.
53. Liu K, Li M, Li Y, Li Y, Chen Z, Tang Y, et al. A review of the clinical efficacy of FDA-approved antibody−drug conjugates in human cancers. *Mol Cancer* 2024;**23**:1−16.
54. Beck A, Terral G, Debaene F, Wagner-Rousset E, Marcoux J, Janin-Bussat MC, et al. Cutting-edge mass spectrometry methods for the multi-level structural characterization of antibody−drug conjugates. *Expert Rev Proteomics* 2016;**13**:157−83.
55. He J, Yu SF, Yee S, Kaur S, Xu K. Characterization of *in vivo* biotransformations for trastuzumab emtansine by high-resolution accurate-mass mass spectrometry. *mAbs* 2018;**10**:960−7.
56. Larson EJ, Zhu Y, Wu Z, Chen B, Zhang Z, Zhou S, et al. Rapid analysis of reduced antibody drug conjugate by online LC−MS/MS with fourier transform ion cyclotron resonance mass spectrometry. *Anal Chem* 2020;**92**:15096−103.
57. Davis JA, Kagan M, Read J, Walles M, Hatsis P. Immunoprecipitation middle-up LC−MS for *in vivo* drug-to-antibody ratio determination for antibody−drug conjugates. *Bioanalysis* 2017;**9**:1535−49.